Localized modulation of rotating waves in Taylor-Couette flow

J. Abshagen,* J. von Stamm, M. Heise,† Ch. Will, and G. Pfister
Institute of Experimental and Applied Physics, University of Kiel, 24098 Kiel, Germany
(Received 15 August 2011; published 18 May 2012)

We report the results of an experimental study on the multiplicity of states in Taylor-Couette flow as a result of axial localization of azimuthally rotating waves. *Localized* states have been found to appear hysteretically from time-dependent Taylor-Couette flow at Reynolds numbers significantly above the onset of wavy Taylor vortices. These *localized* states have the shape of a modulated rotating wave and differ significantly from *global* modulated wavy Taylor vortex states in their spatial characteristics. Axial localization of rotating waves is accompanied with a significant increase in size of the underlying pair of Taylor vortices. Our work reveals that localization provides a mechanism for the appearance of multiple *time-dependent* states in Taylor-Couette flow.

DOI: 10.1103/PhysRevE.85.056307 PACS number(s): 47.20.Ky, 47.20.Qr, 05.45.−a

I. INTRODUCTION

The multiplicity of states, i.e., the coexistence of states for the same values of external control parameters in nonlinear systems, is important for the organization of complexity in many fluid flows [1–9], such as, e.g., in Taylor-Couette flows [10,11]. Multiple states can appear from symmetry-breaking bifurcations and are involved in organizing complex dynamics, e.g., from homoclinic or heteroclinic bifurcations [12,13]. More recently, multiple states have also been found to appear from subcritical bifurcations accompanied with so-called *homoclinic snaking* [14–16]; i.e., each of the bifurcation branches is related to a spatially *localized* state.

Studies on organizing principles of complexity in fluid flows are well suited in simple flow geometries [17,18] which leave the basic flow invariant under certain symmetries, such as in Taylor-Couette flow [19–21]. This hydrodynamic system consists of a viscous fluid in the gap between an inner and an outer cylinder. Physical realizations of the Taylor-Couette flow are confined in the axial direction, e.g., by nonrotating rigid end walls, and are in that case invariant under axial reflections and azimuthal rotations (see, e.g., [22]).

For *stationary* outer cylinders axisymmetric Taylor cells appear smoothly from basic laminar flow for similar Reynolds numbers as the critical Reynolds number Re_c of the centrifugal instability in circular Couette flow [23]. Multiple bifurcation points related to steady axisymmetric states with different numbers of cells [11] and the appearance of anomalous modes [24], as well as symmetry-breaking pitchfork bifurcations [25], give rise to a considerably high multiplicity of steady axisymmetric states in Taylor-Couette flow even for moderate values of Reynolds number and aspect ratios [11].

At higher Re axisymmetric Taylor vortices become unstable via a Hopf bifurcation toward rotating waves [26–36]. For a radius ratio $\eta = 0.5$, which is used in this study, four different types of rotating waves have been observed, i.e., the *small-jet mode*, the *antijet mode*, the *wavy mode*, and the *core mode* [36]. The *small-jet mode* has also been labeled as *wavy outflow boundary* [19,35] and *subharmonic mode* [34] since the oscillation amplitude is localized in the outward jets and adjacent outward jets oscillate in antiphase; i.e., the flow is axially subharmonic with respect to the period of Taylor vortices (assuming translational invariance). Bifurcations from rotating waves toward quasiperiodic [36–42] or axially asymmetric [43] flow states are essential in more complex bifurcation sequences and the transition to disordered Taylor-Couette flow [20–22,43,44].

While rotating and modulated rotating wave states in Taylor-Couette flow are generically *global* states, i.e., they correspond to states having a discrete translational symmetry in an *idealized* translational invariant system [19], there have been observations of flow states with axially localized dynamics in Taylor-Couette flow. Pfister reported on a *localized*, quasiperiodic state in Taylor-Couette flow where a certain type of a rotating wave occurs axially localized only within single vortex pairs [45]. Dynamics on T^3 tori accompanied with these states have also been investigated [46]. Baxter and Andereck presented observations on axially localized dynamical domains in Taylor-Couette flow [47]. Recently, multiple localized states have been found in counter-rotating Taylor-Couette flow below the centrifugal instability of circular Couette flow. Those states are *steady* and *axisymmetric* and their multiplicity has been related to the homoclinic snaking mechanics [48].

In this article, we present the results of an experimental study on the multiplicity of *time-dependent* flow states as a result of axial localization of *rotating waves*. The modulated rotating wave flow, originally found by Pfister [45], involves an axially localized *large-jet mode*, i.e., an axially harmonic wavy outflow boundary flow (assuming translational invariance), accompanied with a global *small-jet mode*. These states appear over a wide range of aspect ratio Γ at higher Reynolds numbers and result in a considerable high multiplicity of time-dependent states in Taylor-Couette flow.

II. EXPERIMENTAL SETUP

The experimental setup consists of a rotating inner and a nonrotating outer cylinder. The rotating inner cylinder is machined from stainless steel having a radius of $r_1 = (12.50 \pm 0.01)$ mm, while the stationary outer cylinder is made from optically polished glass with a radius of $r_2 = (25.00 \pm 0.01)$ mm. This results in a gap width $d = r_2 - r_1 =$

*Present address: janabshagen@bundeswehr.org; Research Department for Underwater Acoustics and Marine Geophysics (FWG), WTD71, Berliner Straße 115, 24340 Eckernförde, Germany.
†heise@physik.uni-kiel.de

12.50 ± 0.02 mm and a radius ratio $\eta = r_1/r_2 = 0.5$ which is held fixed for all measurements. At top and bottom the fluid is confined by solid end walls which are held fixed in the laboratory frame. The distance between these walls defines the axial height L of the flow which is adjustable within an accuracy of 0.01 mm. The measurements were performed with two different Taylor-Couette apparatus in order to ensure that the observed phenomena do not result from experimental imperfections. Such imperfections are generally unavoidable, though the technical specifications of both apparatus are identical except for the maximal adjustable axial length, i.e., $L_{\max} = 210$ mm for the shorter and $L_{\max} = 640$ mm for the longer apparatus.

Control parameters are the aspect ratio $\Gamma = L/d$ and the Reynolds number, which is $\mathrm{Re} = \frac{2\pi f d r_1}{\nu}$ with f denoting the rotation frequency of the inner cylinder. With a phase-locked loop control an accuracy of $\frac{\Delta f}{f} \propto 10^{-4}$ in the short-term and $\frac{\Delta f}{f} \propto 10^{-7}$ in the long-term average is achieved. As a working fluid within the gap between the two concentric cylinders a silicone oil with a kinematic viscosity $\nu = (10.9 \pm 0.1)$ cSt is used. The uncertainty of ± 0.1 cSt refers to the measurement of the absolute value of kinematic viscosity. The accuracy of ν during a measurement is primarily determined by the temperature variation of the fluid that is thermostatically controlled to $(21.00 \pm 0.01)\,^{\circ}$C. This yields $\Delta\nu = \frac{\partial \nu}{\partial T}|_{21.00\,^{\circ}\mathrm{C}}\,\Delta T \approx 0.0025$ cSt. Though the uncertainty in the absolute value of ν introduces an uncertainty of $\frac{\Delta \mathrm{Re}_{\mathrm{abs}}}{\mathrm{Re}} \propto 10^{-2}$ in the absolute value of Re the variation in Reynolds number with time is within $\frac{\Delta \mathrm{Re}}{\mathrm{Re}} \propto 10^{-4}$ during a measurement. This variation determines the resolution in Re that is achieved in the experiment.

For flow visualization purposes, aluminum flakes with a length of 80 μm are added to the fluid. These measurements are performed by monitoring the system with a charge-coupled-device camera in front of the cylinder recording the luminosity along a narrow axial stripe. The spatiotemporal behavior of the flow is then represented by successive stripes for each time step at a constant φ position leading to continuous space-time plots.

Additionally, we utilize laser doppler velocimetry (LDV) for measurements of the radial (u) and axial (w) velocity locally at a certain position (r,z,φ) within the flow domain. The measurements in this article have always been performed at a fixed radial and azimuthal position (r,φ) and either at a fixed axial position z or while simultaneously axially moving the LDV at a constant speed w_{LDV} within the time t; i.e., each data point represents a certain time t referring to a distinct axial position $z(t)$. The corresponding evaluation algorithm is based on the occurring Doppler shift using a bandpass filter that allows us to study the spatiotemporal behavior of stationary and oscillatory flow. In particular the (narrow) bandpass filtering of the so-called axial scans allows to decompose the (spatial) time series into stationary pattern and axially traveling waves, e.g., axisymmetric Ekman vortices and nonaxisymmetric spiral vortices (see [49] for details).

III. RESULTS

A. Flow state with a localized rotating wave

In Fig. 1 space-time plots which are the result of flow visualization measurements of time-dependent flow states are depicted. While in Fig. 1(a) a space-time plot of a global small-jet state is shown, a flow state having a large oscillation amplitude *localized* in a single Taylor vortex pair (here within the fourth vortex pair from bottom) is depicted in Fig. 1(b). The measurement was performed at (a) $\mathrm{Re} = 420$ and (b) $\mathrm{Re} = 1100$, respectively, from states having $N = 12$ vortices at $\Gamma = 11$. This Re is well above the critical one for the onset of rotating waves at this aspect ratio. The flow visualization technique used here represents radially and axially dominated flow as dark and light zones, respectively. Therefore the dark horizontal lines in Fig. 1 result from (almost) stationary inflow boundaries between Taylor vortex pairs. The outflow boundary is also represented by a dark area, but this can be seen to be wavy in Fig. 1 for all cell pairs (the amplitude at the end cells pairs is much smaller than the one in the bulk). These flow states therefore belong to the type of *wavy outflow boundary* or *jet mode*.

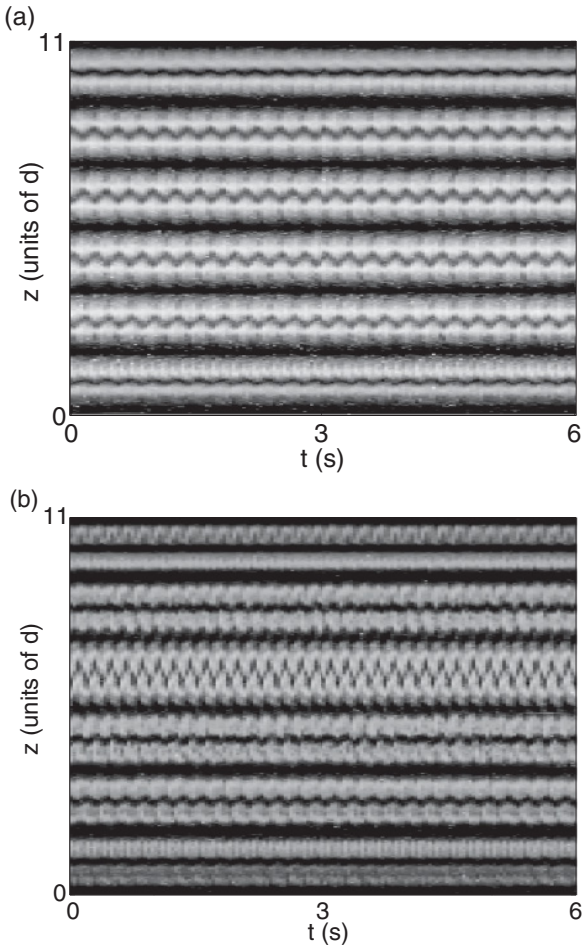

FIG. 1. Space-time plot obtained from flow visualization of (a) a small-jet state and (b) a *localized* large-jet state $^{12}\mathrm{LJ}_4$ with $N = 12$ vortices at $\Gamma = 11$ for $\mathrm{Re} = 420$ and 1100, respectively. Due to the alignment of suspended aluminum flakes the inflow and outflow boundaries appear almost dark in these visualizations while vertically aligned flakes in up- and downward flow reflect incoming light. The wavy structure of the outward flow in the bulk vortex pairs can be seen in both (a) and (b) while inflow boundaries are (almost) stationary. The fourth outflow boundary (from bottom) in (b) exhibits a localized modulation having a very large amplitude.

In order to characterize *localized* flow states it is useful to add an index corresponding to the *localized* oscillatory cell pairs to the label of the mode. Time-dependent flow states are therefore labeled by ${}^{N}(\text{label})_i$, where N reflects the number of cells, (label) is an abbreviation, e.g., for small jet (SJ) or large jet (LJ), and the index i represents the binary coded position of the oscillation of the specific mode in an outflow boundary within the vortex column. Counting from top to bottom, a 1 reflects an oscillatory cell pair with respect to a mode given by (label) while the absence of such oscillation is indicated by 0. The flow state shown in Fig. 1 has only a single cell pair oscillating in a large-jet mode located in the fourth cell pair from below. Since the Ekman vortex pairs are (almost) stationary and three bulk pairs are oscillating in the global small-jet mode, the flow state illustrated in Fig. 1(b) is labeled by ${}^{12}\text{LJ}_{000100}$ or in decimal representation ${}^{12}\text{LJ}_4$.

A close inspection of the axial phases and oscillation frequencies confirms that the flow state is a combination of a small-jet mode and a large-jet mode. The rotation speeds of both types, i.e., the small-jet mode and the large-jet mode, have been previously investigated for the global states and are found to have an almost fixed ratio to the rotation of the inner cylinder ω_i. For the small-jet mode this ratio is within $\omega/\omega_i = 0.46$–0.52 and for the large-jet mode $\omega/\omega_i = 0.54$–0.60 [36]. The wave speeds observed here for both modes within the *localized* states are slightly below these values. For instance, at $\Gamma = 11.07$ and $\text{Re} \approx 900$ both modes have values comparable to the lower limit given in [36], i.e., 0.453 and 0.537, respectively. These values reduce monotonically to 0.433 and 0.533, respectively, at $\text{Re} \approx 1200$ and only show a weak dependence on the aspect ratio.

In order to analyze the *localization* in the spatial amplitude distributions within a time-dependent flow state a decomposition method based on bandpass filtering of the (Doppler-shifted) spectrum and on Hilbert transform is applied to the axial scans using LDV (see, e.g., [49] for details of the method). Figure 2(a) depicts an axial scan, i.e., a time series $u(r = 2\text{ mm}, \varphi, v_{\text{scan}}t, t)$, of a localized large-jet state measured at $\Gamma = 11.1$ and $\text{Re} = 1250$. The broadening results from the speed of the LDV, v_{scan}, which is adjusted in a way that it is much slower than the typical time scale of the slowest time-dependent mode. Note that the oscillations in the axial scan are not resolved on the scale used in Fig. 2 (and also in the following representations of axial scans). The broadening also reflects the amplitude of an oscillation and therefore an axial scan can be considered as a reasonable estimate of an axial amplitude distribution of a mode. Within the axial scan depicted in Fig. 2 the axisymmetric ($m = 0$) component obtained for a decomposition analysis is added as a white line. The flow state depicted in Fig. 2 is the reflection symmetric conjugate state ${}^{12}\text{LJ}_8$ to the state ${}^{12}\text{LJ}_4$ visualized in Fig. 1(b).

The spatial amplitude distribution of a large-jet and a small-jet mode is illustrated in Fig. 2(b). Here, the localization of the large-jet mode [dark gray (online: blue) line] with an amplitude maximum within a single vortex pair and a strong decay in amplitude away from that pair is clearly visible. Moreover, the amplitude of the small-jet mode almost vanishes within this vortex pair and grows away from that pair; i.e., a *hole* is formed in the amplitude distribution of the small-jet mode. At a sufficient axial distance from the localized large-jet mode, e.g., here in the most upper bulk vortex pair, the flow is dominated by the underlying small-jet mode.

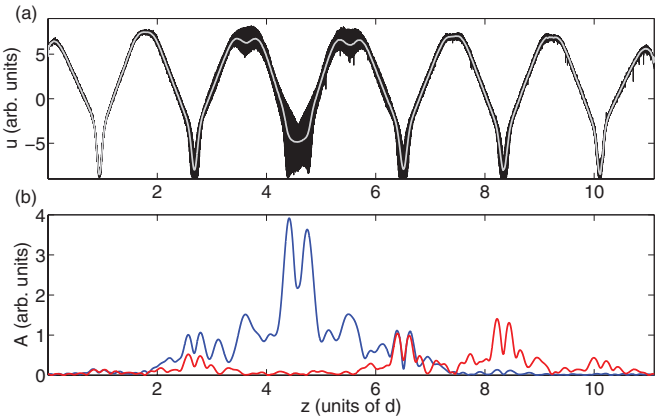

FIG. 2. (Color online) (a) Axial scan of a *localized* large-jet state ${}^{12}\text{LJ}_8$, i.e., the reflection symmetric conjugates state to ${}^{12}\text{LJ}_4$ depicted in Fig. 1, at $\text{Re} = 1250$ and $\Gamma = 11.1$ obtained from (slow) axial movement of the LDV from top ($z = L$) to bottom ($z = 0$) while simultaneously measuring the radial velocity u at 2 mm from the inner cylinder, i.e., $u(r = 2\text{ mm}, \varphi, v_{\text{scan}}t, t)$ with scan velocity v_{scan}. (b) Mode amplitudes of the small jet in light gray (red) and the large jet in dark gray (blue) obtained from the Hilbert transform of the (Doppler-shifted) band-pass filtered spectrum. *Localization* of the large-jet mode and the *hole* of the small-jet mode is clearly visible.

Localization in the axial cell size (corresponding to the axial wave number) distribution is analyzed by LDV measurements. Therefore the size of cell pairs is measured from the axial position of the inflow boundaries. A mean of the radial position of the streamline with a zero axial velocity component provides an accurate measure for an inflow boundary. It is therefore measured at seven different radial positions, $r = [1,2,3,9,10,11,12]$ mm, from the inner cylinder by a comparison of the measured frequencies with the frequency shift of the LDV. In Fig. 3 the cell size distribution of a localized large-jet state ${}^{12}\text{LJ}_4$ $(*, \lambda_{x,1-6})$ and of the reflection symmetric conjugate state ${}^{12}\text{LJ}_8(o, \lambda_{1-6,x})$ at $\Gamma = 11.53$ is depicted. It can be seen that the size of the cell pairs and their conjugate ones are almost identical. A *localized* large-jet mode within a cell pair results in a significant increase in the axial cell size of that pair. In particular these pairs are larger than the bulk pairs where the small-jet mode is dominating. Note that an interaction of the rotating wave and the underlying cell pair has also been found for wavy Taylor vortex flow [50,51]. The *localized* increase in cell pair size due to the large-jet mode is accompanied with a decrease in the size of the Ekman cell pairs. The dependence of the cell size distribution from Re reveals a correspondence between the *localized* cell pair of large-jet mode and the Ekman cell pairs. Growth (or decay) in size with Re is limited to those pairs. The remaining bulk pairs do not change significantly in size with Re and are only shifted in axial position.

Axial scans of five different eight-cell flows are depicted in Fig. 4. The axial velocity w was for each measurement recorded at a radial distance of 9 mm from the inner cylinder. The small-jet mode appears only in the *global* state ${}^{8}\text{SJ}_6$; i.e., except for the Ekman cell pairs the bulk pairs only oscillate in the small-jet mode. Such a *global* state also exists for the

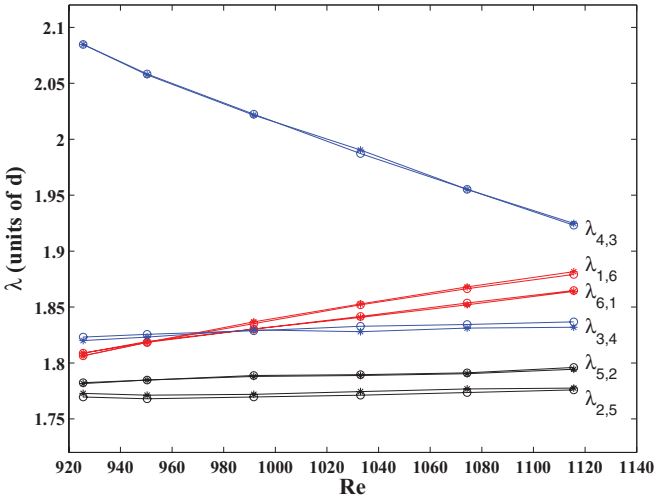

FIG. 3. (Color online) Cell pair size distribution of $^{12}LJ_4$ ($*$,$\lambda_{x,1-6}$) and $^{12}LJ_8$ ($\bigcirc$,$\lambda_{1-6,x}$) at $\Gamma = 11.53$ (cell pair size λ is labeled in ascending order from bottom to top). Cell pairs with large-jet waves [dark gray (blue) line] are significantly larger than bulk pairs (black line). End pairs [light gray (red) line] and cell pairs oscillating localized in the large-jet mode [dark gray (blue) line] have a size dependence on Re.

large-jet mode. This eight-cell state is labeled $^8LJ_6$ and is represented by the axial scan in Fig. 4. Axial scans of two states with *localized* large-jet modes, i.e., $^8LJ_2$ and $^8LJ_4$, can also be seen in Fig. 4. Both are conjugate states with respect to the axial reflection symmetry. Since end cells have not been found to oscillate in large-jet mode, only these two *localized* large-jet states exist in an eight-cell flow. Therefore the flow states as represented in Fig. 4 can be considered as a complete set of large-jet states. Note that for flow states having less than four outward jets, i.e., eight-cell, the large-jet mode is not found to exist as a *localized* mode.

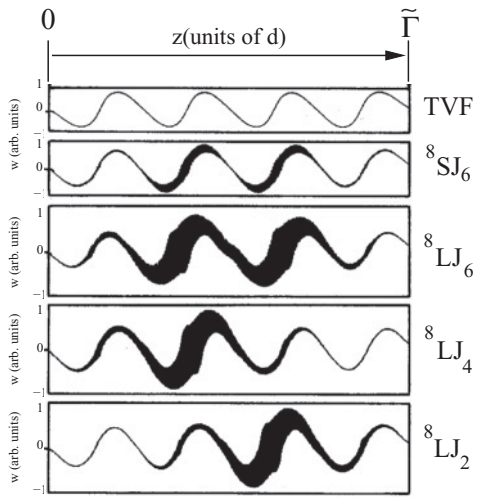

FIG. 4. Axial scans $w(r = 9\,\text{mm},\varphi,v_{\text{scan}}t,t)$ from five different flow states with eight cells (from top to bottom): steady Taylor vortex flow (TVF), *global* small-jet state $^8SJ_6$, *global* large-jet state $^8LJ_6$, *localized* large-jet state $^8LJ_4$, and its conjugate state $^8LJ_2$ with respect to reflection symmetry.

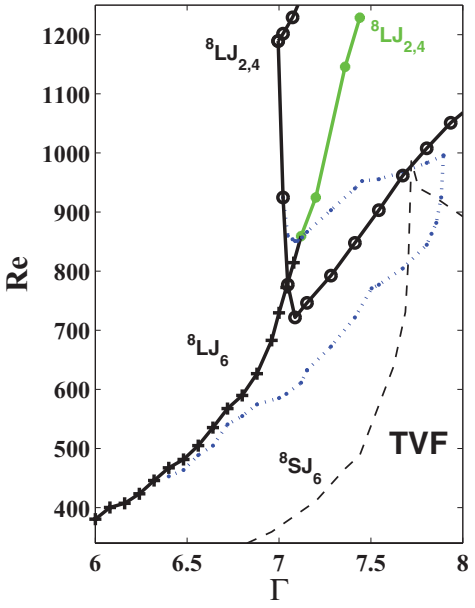

FIG. 5. (Color online) Stability diagram of large-jet states with eight cells: transition to the *global* large-jet state $^8LJ_6$ (+, black line) and vice versa [dotted dark gray (blue) line], transition to the *localized* large-jet states $^8LJ_{2,4}$ [•, light gray (green) line] and vice versa ($\circ$, solid black line), and (dashed black line) the onset of rotating wave $^8SJ_6$ and *antijet* mode from steady Taylor vortex flow below and above $\Gamma = 7.7$, respectively.

B. Stability of axially localized states

A part of the eight-cell flow stability diagram is depicted in Fig. 5, where the aspect ratio Γ is restricted to $6 \leqslant \Gamma \leqslant 8$; i.e., the cells are *compressed* with respect to the critical wavelength of Taylor cells in an axially periodic system. A time-dependent instability of Taylor vortex flow (TVF) within this regime results in the appearance of a rotating wave [36]; i.e., the small-jet state $^8SJ_6$ is represented in Fig. 4 (above $\Gamma \geqslant 7.7$ a so-called *antijet* state or *wavy inflow boundary* [19]). The Hopf bifurcation toward the rotating waves in Taylor vortex flow is indicated in Fig. 5 as a dashed line. Axisymmetric instabilities of the rotating wave $^8SJ_6$, such as the steady symmetry-breaking and the bifurcation behavior of the very-low-frequency mode [36,43,44], are omitted in Fig. 5 for reasons of clarity.

Increasing Re quasistatically above the black lines (+) or light gray (online: green) lines (•), the *basic* time-dependent flow, that consists of a small-jet mode and axisymmetric dynamics, undergoes a transition toward the *global* state $^8LJ_6$ or one of the *localized* $^8LJ_{2,4}$ states, respectively. While the *global* state retains the axial reflection symmetry, it is broken at the onset of a *localized* state. Both *global* and *localized* states appear with a finite amplitude from this *hysteretic* transition. The dash-dotted dark gray (online: blue) line indicates the region of existence of the global state $^8LJ_6$ below its onset, while the black line ($\circ$) represents the lower stability border of both *localized* states $^8LJ_{2,4}$. Within the experimental accuracy the stability borders of the *localized* states are identical.

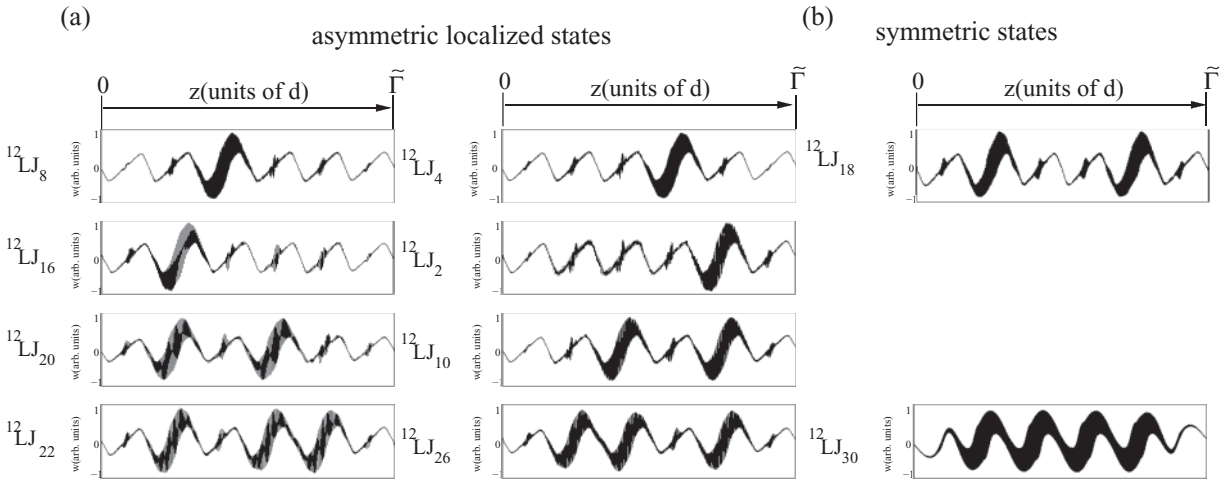

FIG. 6. Axial scans $w(r = 9\,\mathrm{mm}, \varphi, v_{\mathrm{scan}}t, t)$ obtained from *localized* large-jet states and the *global* large-jet state with $N = 12$ cells. Large-jet states are either (a) asymmetric or (b) symmetric with respect to the axial reflection symmetry.

C. Multiplicity of localized states

Since the large-jet mode is only found to oscillate *localized* in the outward jet of a cell pair within the bulk of the flow, i.e., not within an Ekman cell pair, the number of possible *localized* states, as described above, is restricted to two in an eight-cell (four-jet) flow. The possible number of *localized* states increases significantly as the number of underlying Taylor cells is greater than eight. For instance, at a twelve-cell flow (six outward jets) the possible number of localized states is 14 (if no oscillation within an Ekman cell pair is assumed and the global state is omitted). The experimentally observed *localized* large-jet states (and the global large-jet state) are illustrated in Fig. 6. It can be seen that all possible *localized* states having just a single cell pair oscillating in large-jet mode but not all of the possible *localized* states with more than one large-jet oscillation have also been observed.

It is apparent from Fig. 6 that both types of *localized* large-jet states either breaking or retaining the axial reflection symmetry have been observed. Therefore, in contrast to the eight-cell flow, localization is not necessarily accompanied with the breaking of the reflection symmetry for the twelve-cell flow. Note that for each *localized* large-jet state the conjugate state with respect to reflection symmetry has also been observed.

For $N = 12$ the onset of the small-jet mode from Taylor cells occurs for almost the same critical Re as for $N = 8$ [36]. The stability border of the *global* small-jet state $^{12}\mathrm{SJ}_{30}$ (and the antijet state for larger aspect ratios) is indicated as a dashed black line in the stability diagram in Fig. 7. Increasing Re from the small-jet state results in a transition to different large-jet states. The *basic* time-dependent state from which the transition occurs consists of the small-jet mode and axisymmetric dynamics [36,43,44]. The bifurcation behavior of the axisymmetric time-dependent flow is omitted for reasons of clarity in Fig. 7 (as in Fig. 5 for eight-cell flow). Depending on the aspect ratio either the *global* large-jet state $^{12}\mathrm{LJ}_{30}$ or one of the *localized* states $^{12}\mathrm{LJ}_{4,8,10,18,20,22,26}$ occurs from this transition. In particular not all possible states have been found to occur from the *basic* time-dependent state by a quasistatical increase of Re. However, those states, i.e., $^{12}\mathrm{LJ}_{2,16}$, can be reached by sudden starts from a lower Reynolds number, i.e., by imposing a strong perturbation to the *basic* time-dependent flow or in a transition from one of the other localized states.

It can be seen from Fig. 7 that for $N = 12$ the localized large-jet states occur in a similar parameter regime of aspect ratio (normalized to N) and Re as the *localized* states with eight cells. The lower stability curve of $^{12}\mathrm{LJ}_{4,8}$, i.e., *localized* states having a single large-jet oscillation in one of the midcell pairs, is represented in Fig. 7 by ○ (black line). The stability

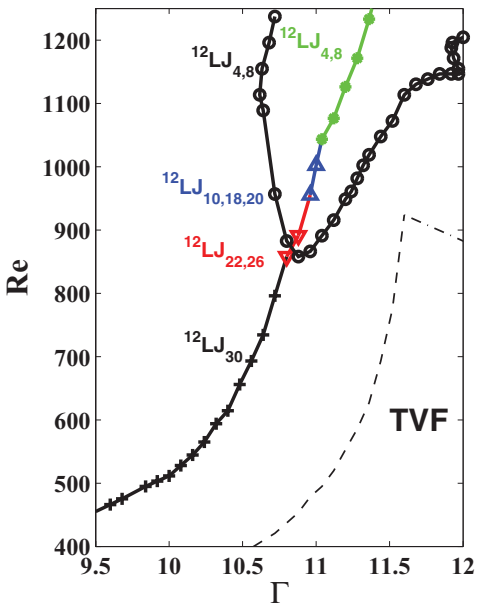

FIG. 7. (Color online) Stability diagram of the large-jet states with twelve cells: transition to *global* large-jet $^{12}\mathrm{LJ}_{30}$ (+, black line) and to localized large-jet states $^{12}\mathrm{LJ}_{22,26}$ (▽, black line), $^{12}\mathrm{LJ}_{10,18,20}$ [△, dark gray (blue) line], and $^{12}\mathrm{LJ}_{4,8}$ [•, light gray (green) line]; lower stability boundary of localized large-jet states $^{12}\mathrm{LJ}_{4,8}$ (○, black line); and onset of rotating waves (small-jet state $^{12}\mathrm{SJ}_{30}$ and for $\Gamma > 11.6$ antijet state) in a steady Taylor vortex flow (dashed black line).

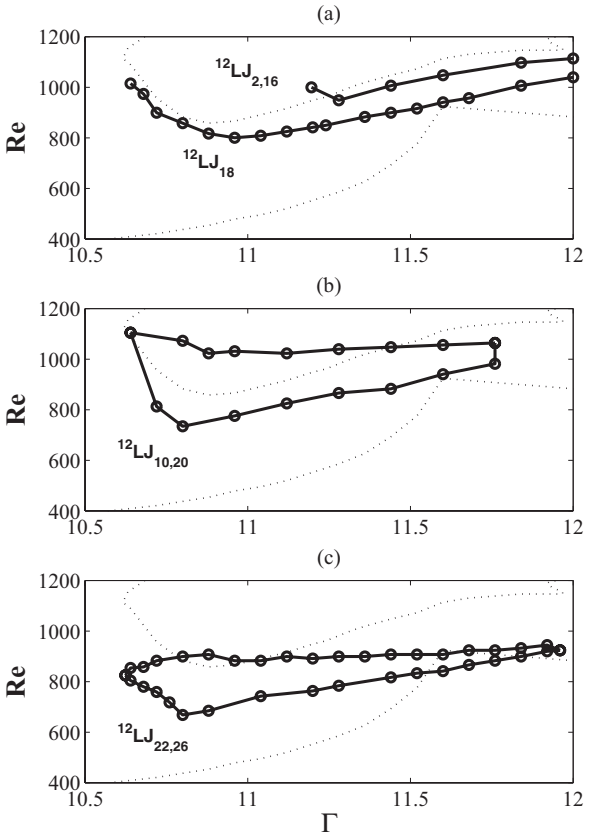

FIG. 8. (a) Lower stability border of localized large-jet states ^{12}LJ$_{18}$ and ^{12}LJ$_{2,16}$. Stability boundary of localized large-jet states (b) ^{12}LJ$_{10,20}$ and (c) ^{12}LJ$_{22,26}$ (indicated as solid black lines). Onset of time dependence in a Taylor vortex flow and lower stability boundary of localized large-jet ^{12}LJ$_{4,8}$ are added for comparison (dotted lines).

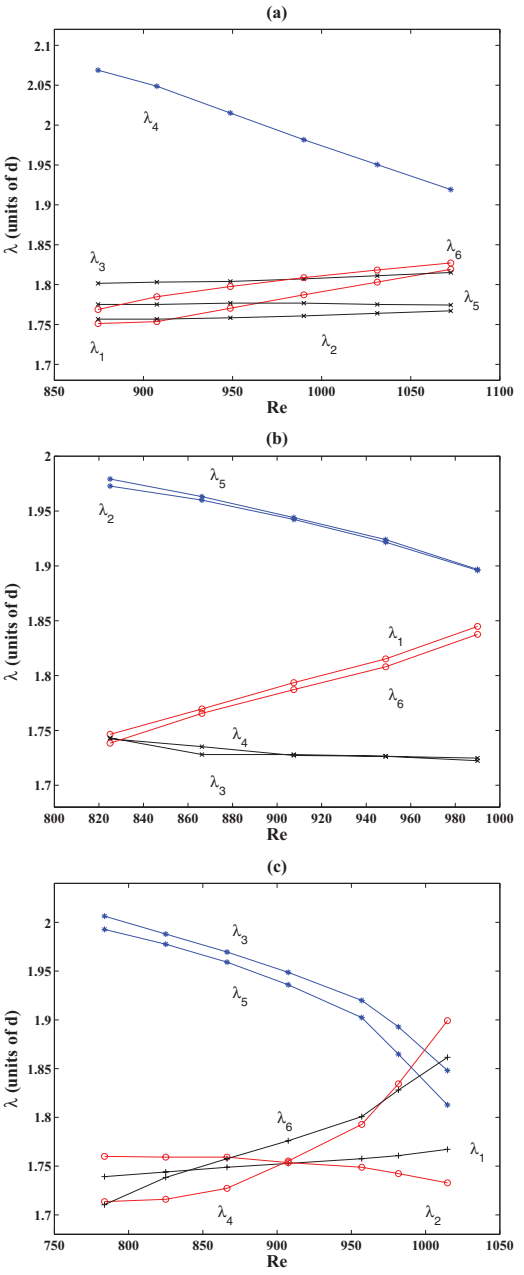

FIG. 9. (Color online) Distribution of the cell pair size λ for (a) ^{12}LJ$_4$, (b) ^{12}LJ$_{18}$, and (c) ^{12}LJ$_{10}$ at Γ = 10.92 (labeled in ascending order from bottom to top). Cell pairs oscillating in large-jet mode [∗, dark gray (blue) line] are significantly larger than bulk pairs (×, black line). End pairs $\lambda_{1,6}$ [○, light gray (red) line] and localized large-jet cell pairs vary significantly in size with Re.

borders of both conjugate *localized* states have also been found to be identical within our accuracy.

The stability regime of the other *localized* large-jet states with $N = 12$ is depicted in Fig. 8. For comparison the onset of time dependence in Taylor vortex flow as well as the stability border of ^{12}LJ$_{4,8}$ is added in each plot. In Fig. 8(a) the lower stability border of the *localized* large-jet states ^{12}LJ$_{2,16}$, i.e., the other type of state having only a single oscillating outward jet in large-jet mode, is depicted. The border is located slightly below the critical Reynolds number of ^{12}LJ$_{4,8}$ but disappears already at larger values of Γ (the stability border has been traced only to Re ≈ 1000 to illustrate the principle behavior). The lower stability curve of the symmetric state ^{12}LJ$_{18}$ has a similar shape to the one of ^{12}LJ$_{4,8}$ over the entire regime of aspect ratio but it is systematically shifted toward lower Reynolds numbers. The upper stability curve of the localized states ^{12}LJ$_{2,4,8,12,18}$ is above $1100 \lesssim Re \lesssim 1200$ for all aspect ratios we investigated and therefore just the lower part of the curve is depicted in Figs. 7 and 8(a) for these states. For Re above those values the flow typically becomes disordered and will not be discussed here.

The stability regime of the *localized* large-jet states ^{12}LJ$_{10,20,22,26}$ is depicted in Figs. 8(b) and 8(c). These *localized* states still form a torus of small-jet mode and large-jet mode at the upper stability border and the stability regime forms a closed patch within the parameter space (Re, Γ). The patch for the states with three localized oscillations [^{12}LJ$_{22,26}$, Fig. 8(c)] exists at lower Re compared to the patch with two [^{12}LJ$_{10,20}$, Fig. 8(b)]. *Localized* states with more numbers of oscillations are found to be stable toward lower Re in general. It can be seen, however, that there exists a large parameter regime of coexistence of the *localized* states and therefore a high multiplicity of states that results for localization of rotating waves within the outward jets.

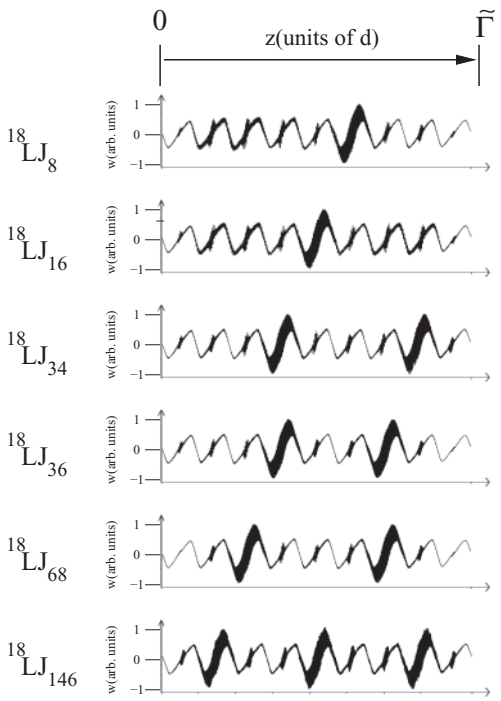

FIG. 10. Selection of localized large-jet states with $N = 18$ cells represented by axial scans. Both symmetric ($^{18}LJ_{68,146}$) and asymmetric ($^{18}LJ_{8,16,34,36}$) states have been observed for comparable Re and aspect ratios Γ.

D. Spatial distribution of cell size

An oscillation in the large-jet mode influences the size of the underlying cell pair significantly. The cell size distribution of three different localized large-jet states with $N = 12$ at $\Gamma = 10.92$ is therefore plotted as a function of Re in Fig. 7. The size of cell pairs is determined from the mean axial position of the inflow boundaries estimated from measurements at seven different radial positions, $r = [1,2,3,9,10,11,12]$ mm. Cell pairs oscillating in large-jet mode have a larger size than the other cell pairs in general. This increased size of such cell pairs can be seen in Fig. 9(a) for $^{12}LJ_4$, i.e., a state having a single cell pair oscillating in large-jet mode. Qualitatively the same behavior is found for flow states having two of those pairs, i.e., for the symmetric localized state $^{12}LJ_{18}$ that is depicted in Fig. 9(b) and the asymmetric state $^{12}LJ_{10}$ in Fig. 9(c). The difference in size between cell pairs oscillating in large-jet cell mode and the other pairs is in general the largest at the lower stability boundary and decreases approximately linearly with increasing Re. The decrease in size of cell pairs with large-jet oscillation is accompanied with an increase in size mainly of the end cell pair while the pairs oscillating in small-jet mode are typically much less influenced. Those pairs are shifted in their axial position. Only for $^{12}LJ_{18}$ the size of the cell pair in between the two localized large-jet oscillations increases with Re while one of the end pairs decreases in size. Note that the end cell pairs are typically larger than bulk pairs for Taylor vortex flow at a comparable aspect ratio [43]. It should be further noted that the wave speeds within the asymmetric and the symmetric state $^{12}LJ_{10}$ and $^{12}LJ_{18}$ are identical but both differ from the wave speed of $^{12}LJ_4$.

E. Localized states in larger systems

The multiplicity of states is significantly higher if the number of cell pairs (outward jets) is increased from four to six, i.e., from $N = 8$ to 12 cells. While only a single type of localized state has been found for $N = 8$, the number of different types observed for $N = 12$ has increased to six. The actual number of different states is even higher since the mirror images of each asymmetric state also exist. It can be expected that the number of possible localized states increases drastically for flows having an even larger number of cell pairs. In Fig. 10 axial scans from a selection of localized large-jet states for $N = 18$ are depicted. Those *localized* states, either symmetric or asymmetric, appear for comparable Reynolds numbers and aspect ratios (if normalized to the number of cells) as in smaller systems. Therefore it can be seen that flow states with axially localized rotating waves are also stable in systems with a larger spatial extent and therefore result in a high multiplicity of states.

IV. CONCLUSION

We have reported on a experimental investigation on localized *time-dependent* states in Taylor-Couette flow which exist well above the onset of time dependence. *Localized* states appear hysteretically from symmetry-breaking and symmetry-increasing transitions with respect to axial reflection symmetry. While the existence of localized *time-dependent* states in Taylor-Couette flow is known due to the work of Pfister [45] and Baxter and Andereck [47], we explicitly show that localization results in a high multiplicity of time-dependent states having the form of a modulated rotating wave. Furthermore, axial localizations of rotating waves are found to be accompanied with a significant increase in cell size while the size of Ekman cells decreases. The presence of axial end walls is therefore of relevance for these *localized* states.

Our work reveals that *localization* of rotating waves provides a mechanism for a high multiplicity of states in *non-axisymmetric* Taylor-Couette flow. Since the multiplicity of states has been proven to be crucial for the organization of the complexity in *axisymmetric* Taylor-Couette flow [11,22,25], the multiple *time-dependent* states investigated here may also be expected to be involved in the organization of complex dynamics in this flow system.

ACKNOWLEDGMENTS

We acknowledge support from the Deutsche Forschungsgemeinschaft.

[1] M. Ottaviani, F. Porcelli, and D. Grasso, Phys. Rev. Lett. **93**, 075001 (2004).
[2] J. Yoo, Int. J. Heat Mass Transf. **42**, 709 (1999).
[3] I. B. Konovalov, A. M. Feigin, and A. Mukhina, J. Geophys. Res. **104**, 3669 (1999).
[4] K. Boronska and L. Tuckerman, J. Fluid Mech. **559**, 279 (2006).

[5] B. Hof, P. Lucas, and T. Mullin, Phys. Fluids **11**, 2815 (1999).
[6] D.-J. Ma, D.-J. Sun, and X.-Y. Yin, Phys. Rev. E **74**, 037302 (2006).
[7] A. Heap and A. Juel, Phys. Fluids **20**, 081702 (2008).
[8] X. Lup and T. Pedley, J. Fluid Mech. **420**, 301 (2000).
[9] B. Li, L. Zheng, X. Zhang, and L. Ma, Adv. Studies Theor. Phys. **2**, 473 (2008).
[10] D. Coles, J. Fluid Mech. **21**, 385 (1965).
[11] T. B. Benjamin and T. Mullin, J. Fluid Mech. **121**, 219 (1982).
[12] J. Guckenheimer and P. Holmes, *Nonlinear Oscillations, Dynamical Systems and Bifurcations of Vector Fields* (Springer, New York, 1986).
[13] M. Golubitsky and D. Schaeffer, *Singularities and Groups in Bifurcation Theory* (Springer, New York, 1988), Vols. 1–2.
[14] E. Knobloch, Nonlinearity **21**, T45 (2008).
[15] I. Mercader, O. Batiste, A. Alonso, and E. Knobloch, Phys. Rev. E **80**, 025201 (2009).
[16] J. Dawes, SIAM J. Appl. Dyns. Sys. **8**, 909 (2009).
[17] M. Cross and P. Hohenberg, Rev. Mod. Phys. **65**, 851 (1993).
[18] H. Swinney and J. Gollub, *Hydrodynamic Instabilities and the Transition to Turbulence* (Springer, New York, 1981).
[19] P. Chossat and G. Iooss, *The Couette-Taylor Problem* (Springer, New York, 1994).
[20] R. Tagg, Nonlinear Sci. Today **4**, 1 (1994).
[21] E. Koschmieder, J. Fluid Mech. **24**, 521 (1966).
[22] T. Mullin, *The Nature of Chaos* (Oxford University Press, Oxford, 1993).
[23] T. Benjamin, Proc. R. Soc. London A **359**, 1 (1978).
[24] K. Cliffe, J. Kobine, and T. Mullin, Philos. Trans. R. Soc. London A **739**, 341 (1992).
[25] T. Mullin and T. Price, Nature (London) **340**, 294 (1989).
[26] T. Mullin and T. Benjamin, Nature (London) **288**, 567 (1980).
[27] T. Mullin, Phys. Rev. A **31**, 1216 (1985).
[28] A. Lorenzen, G. Pfister, and T. Mullin, Phys. Fluids **26**, 10 (1983).
[29] C. Andereck, S. Liu, and H. Swinney, J. Fluid Mech. **164**, 155 (1986).
[30] J. Antonijoan and J. Sánchez, Phys. Fluids **14**, 1661 (2002).
[31] W. Edwards, S. Beane, and S. Varma, Phys. Fluids A **3**, 1510 (1991).
[32] M. Nagata, J. Fluid Mech. **188**, 585 (1988).
[33] P. Marcus, J. Fluid Mech. **146**, 45 (1984).
[34] C. Jones, J. Fluid Mech. **102**, 249 (1981).
[35] G. Iooss, J. Fluid Mech. **173**, 273 (1986).
[36] U. Gerdts, J. von Stamm, T. Buzug, and G. Pfister, Phys. Rev. E **49**, 4019 (1994).
[37] M. Gorman and H. L. Swinney, Phys. Rev. Lett. **43**, 1871 (1979).
[38] K. T. Coughlin, P. S. Marcus, R. P. Tagg, and H. L. Swinney, Phys. Rev. Lett. **66**, 1161 (1991).
[39] K. Coughlin and P. Marcus, J. Fluid Mech. **234**, 1 (1992).
[40] K. Coughlin and P. Marcus, J. Fluid Mech. **234**, 19 (1992).
[41] M. Gorman and H. Swinney, J. Fluid Mech. **117**, 123 (1982).
[42] L.-H. Zhang and H. L. Swinney, Phys. Rev. A **31**, 1006 (1985).
[43] J. von Stamm, U. Gerdts, T. Buzug, and G. Pfister, Phys. Rev. E **54**, 4938 (1996).
[44] J. Abshagen, G. Pfister, and T. Mullin, Phys. Rev. Lett. **87**, 224501 (2001).
[45] G. Pfister, in *4th Int. Conf. on Photon Correlation Techniques in Fluid Mechanics* (Joint Institute for Aeronautics and Acoustics, Stanford, USA, 1980), pp. 159–169.
[46] J. Abshagen and G. Pfister, in *Physics of Rotating Fluids*, edited by C. Egbers and G. Pfister (Springer, Berlin, 2000), pp. 84–100.
[47] G. W. Baxter and C. D. Andereck, Phys. Rev. Lett. **57**, 3046 (1986).
[48] J. Abshagen, M. Heise, G. Pfister, and T. Mullin, Phys. Fluids **22**, 021702 (2010).
[49] M. Heise, J. Abshagen, D. Küter, K. Hochstrate, G. Pfister, and C. Hoffmann, Phys. Rev. E **77**, 026202 (2008).
[50] G. Bust, B. Dornblaser, and E. Koschmieder, Phys. Fluids **28**, 1243 (1985).
[51] J. Abshagen and G. Pfister, Phys. Rev. E **78**, 046206 (2008).